2D models for dust-driven AGB star winds

Woitke, P.

A&A 452, 537–549 (2006)
DOI: 10.1051/0004-6361:20054202

Astronomy & Astrophysics

2D models for dust-driven AGB star winds

P. Woitke

Sterrewacht Leiden, PO Box 9513, 2300 RA Leiden, The Netherlands
e-mail: woitke@strw.leidenuniv.nl

Received 14 September 2005 / Accepted 1 March 2006

ABSTRACT

New axisymmetric (2D) models for dust-driven winds of C-stars are presented which include hydrodynamics with radiation pressure on dust, equilibrium chemistry and time-dependent dust formation with coupled grey Monte Carlo radiative transfer. Considering the simplest case without stellar pulsation (hydrostatic inner boundary condition) these models reveal a more complex picture of the dust formation and wind acceleration than earlier published spherically symmetric (1D) models. The so-called exterior κ-mechanism causes radial oscillations with short phases of active dust formation between longer phases without appreciable dust formation, just like in the 1D models. However, in 2D geometry, the oscillations can be out-of-phase at different places above the stellar atmosphere which results in the formation of dust arcs or smaller caps that only occupy a certain fraction of the total solid angle. These dust structures are accelerated outward by radiation pressure, expanding radially and tangentially like mushroom clouds, while dust-poor matter is falling back towards the star at other places. A highly dynamical and turbulent dust formation zone is created in this way, which again leads to inhomogeneous dust production. Further away from the star, flow instabilities (e.g. Rayleigh-Taylor) have time to fragment the outward moving arcs and shells to produce numerous small-scale cloud-like sub-structures.

Key words. hydrodynamics – radiative transfer – instabilities – stars: winds, outflows – stars: mass-loss – stars: AGB and post-AGB

1. Introduction

Asymptotic Giant Branch (AGB) stars are known to generate massive stellar winds with mass loss rates up to $10^{-4}\,M_\odot$/yr (Habing 1996; LeBertre 1997; Wallerstein & Knapp 1998), which drives them towards the planetary nebula phase. According to the currently available spherically symmetric (1D) model calculations (Winters et al. 2000; Höfner et al. 2003; Sandin & Höfner 2003; Schirrmacher et al. 2003), these winds are driven by a combination of stellar pulsation and radiation pressure on dust grains. An exterior κ-mechanism leads to the production of radial dust shells in more or less regular long time intervals, even if the pulsation of the star is neglected in the model (Fleischer et al. 1995; Höfner et al. 1995).

The formation of radial dust shells, however, does not seem to be in general agreement with recent interferometric observations. Infrared speckle observations have clearly indicated that the innermost dust distribution around red giants can deviate strongly from spherical symmetry (Weigelt et al. 2002; Monnier et al. 2004; Tuthill et al. 2005) with evidence for moving clouds, arcs and "bars". The new IR VLTI instruments AMBER and MIDI will allow for an even more detailed view on the dust formation and wind acceleration zones of AGB stars with the ability to detect wind asymmetries and cloud-like inhomogeneities, and to track individual dust shells or clouds.

These observations call for likewise detailed 3D models. Without such models, the interpretation of the new interferometric data will necessarily remain on a more or less phenomenological level which is unsatisfactory because it leaves most of the important physical questions unanswered.

The major aim of this work is to advance from 1D to 2D dust-driven wind models. These models will enable us to discuss whether dust-driven winds remain spherically symmetric (if the initial and boundary conditions are spherically symmetric) or whether instabilities lead to spontaneous symmetry breaking, structure formation and more complex flow patterns, which might explain the observed irregular dust structures. Post-processing of the model results will allow us to calculate simulated images and visibilities (see Woitke & Quirrenbach 2005) which can be directly compared to observations.

2. The model

2.1. The equations

The dust-driven stellar wind is described by the equation of continuity (Eq. (1)), the equation of motion (Eq. (2)), the gas energy equation (Eq. (3)), a system of moment equations describing the time-dependent formation of dust particles from the gas phase (Eq. (4)), and the radiative transfer equation (Eq. (5)):

$$\frac{\partial\rho}{\partial t} + \nabla(\rho\boldsymbol{v}) = 0 \tag{1}$$

$$\frac{\partial}{\partial t}\Big(\rho\boldsymbol{v}\Big) + \nabla\Big(\rho\boldsymbol{v}\circ\boldsymbol{v} + p\Big) = \rho\left(\boldsymbol{a}_{\rm rad} - \boldsymbol{a}_{\rm grav}\right) \tag{2}$$

$$\frac{\partial}{\partial t}\Big(\rho e\Big) + \nabla\Big([\rho e + p]\boldsymbol{v}\Big) = \rho\boldsymbol{v}\cdot\left(\boldsymbol{a}_{\rm rad} - \boldsymbol{a}_{\rm grav}\right) + \rho\, Q_{\rm rad} \tag{3}$$

$$\frac{\partial}{\partial t}\Big(\rho L_j\Big) + \nabla\Big(\rho L_j\boldsymbol{v}\Big) = {V_\ell}^{j/3} J_\star + \frac{j}{3}\chi^{\rm net}\rho L_{j-1} \tag{4}$$

$$\boldsymbol{n}\cdot\nabla I_\nu(\boldsymbol{r},\boldsymbol{n}) = \eta_\nu(\boldsymbol{r},\boldsymbol{n}) - \kappa_\nu^{\rm ext}(\boldsymbol{r})\, I_\nu(\boldsymbol{r},\boldsymbol{n}) \tag{5}$$

ρ is the mass density, $e = e_{\rm int} + e_{\rm kin}$ the internal (including kinetic) gas energy and p the thermal gas pressure. $\boldsymbol{a}_{\rm grav}$ is the gravitational deceleration and $\boldsymbol{a}_{\rm rad}$ the acceleration by radiation pressure on dust and gas. $Q_{\rm rad}$ is the net energy exchange rate of the gas with the radiation field (negative for radiative cooling). $I_\nu(\boldsymbol{r},\boldsymbol{n})$ is the spectral intensity at point $\boldsymbol{r}$ in direction of

the unit vector $\boldsymbol{n}$, $\eta_\nu(\boldsymbol{r},\boldsymbol{n})$ the total emission coefficient (including scattering) and $\kappa_\nu^{\rm ext}(\boldsymbol{r})$ the extinction coefficient. For further explanations of the introduced quantities see Sects. 2.3 and 2.4.

The dust/gas mixture is approximated by a single hydrodynamic fluid with bulk velocity $\boldsymbol{v}$ (see Simis et al. 2001; and Sandin & Höfner 2003, for the effects of dust drift velocities in 1D models). However, since dust and gas are known to decouple thermally from each other easily under the predominant conditions in red giant winds (e.g. Woitke et al. 1999), two distinct temperatures are introduced, namely the gas temperature $T_{\rm g}$ and the dust temperature $T_{\rm d}$. Whereas $T_{\rm g}$ is a result of the solution of the gas energy equation (Eq. (3)), we assume that the dust temperature $T_{\rm d}$ relaxes instantaneously to its local radiative equilibrium value, which is part of the results of our radiative transfer treatment (see Sect. 2.4).

2.2. Hydrodynamics

The multi-dimensional models are developed in the frame of the FLASH 2.4 hydrocode (Fryxell et al. 2000), which is an explicit, finite volume, high-order Godunov-type hydro-solver which uses Adaptive Mesh Refinement (AMR) and is fully parallel (MPI). Spherical coordinates (r,θ,ϕ) are used either in 1D (spherically symmetric models) or 2D (axisymmetric models).

The source terms appearing on the r.h.s. of the hydro-equations (Eqs. (1) to (4)) are treated by operator splitting, where the time-integration is carried out by means of the implicit extrapolation solver LIMEX 4.2A1 (Deuflhard & Nowak 1987).

Gravity and radiation pressure are calculated by

$$\boldsymbol{a}_{\rm rad} - \boldsymbol{a}_{\rm grav} = \left(\frac{\widehat{\kappa}_{\rm ext} L_\star}{4\pi r^2 c} - \frac{GM_r}{r^2}\right)\boldsymbol{e}_r, \tag{6}$$

where $\boldsymbol{e}_r$ is the unit vector in the radial direction, G the constant of gravity, $L_\star$ the stellar luminosity, $\widehat{\kappa}_{\rm ext}$ the grey (dust + gas) extinction coefficient per unit mass and c the speed of light. The enclosed mass is approximated by $M_r \approx M_r(t=0)$, i.e. we assume a constant spherically symmetric gravitational potential as calculated for the initial state. The radiation pressure is assumed to be strictly directed into the radial direction. The calculation of the sideway radiation pressure by the Monte Carlo radiative transfer method (see Sect. 2.4) would be possible, but the results are too noisy. Using these results could introduce spurious numerical instabilities.

Net radiative heating of the gas is calculated by

$$Q_{\rm rad} = 4\sigma\widehat{\kappa}_{\rm abs}^{\rm gas}\left(T_{\rm rad}^4 - T_{\rm g}^4\right), \tag{7}$$

assuming LTE, where $\widehat{\kappa}_{\rm abs}^{\rm gas}$ is the gas absorption coefficient per mass and $T_{\rm rad}$ is a measure for the mean intensity ($J = \frac{\sigma}{\pi}T_{\rm rad}^4$, see Sect. 2.4).

As equation of state, we apply the ideal gas law for atomic hydrogen with $\gamma = 5/3$ (disregarding H_2), i.e. $p = \frac{k}{\bar{\mu}}\rho T_{\rm g}$ and $e_{\rm int} = \frac{1}{\gamma-1}p/\rho$, where k is the Boltzmann constant and $\bar{\mu} = 1.28$ amu the mean molecular mass.

2.3. Chemistry and dust formation

The time-dependent formation of dust in the carbon-rich case is calculated according to the moment method developed by Gail & Sedlmayr (1988), Gauger et al. (1990) and Dominik et al. (1993). Assuming spherical dust particles, the moments of the dust size distribution function $f(V,\boldsymbol{r},t)$ [cm^{-6}] are defined as

$$\rho L_j(\boldsymbol{r},t) = \int_{V_\ell}^{\infty} f(V,\boldsymbol{r},t)\, V^{j/3}{\rm d}V \quad \Big(j \in \{0,1,2,3\}\Big), \tag{8}$$

where L_j has units [cm^j/g]. V [cm^3] is the dust particle volume and V_ℓ the minimum volume of a large molecule to be counted as dust particle. The temporal change of these dust moments, as affected by nucleation, growth and evaporation, are calculated according to Eq. (4). Here, $J_\star$ [cm^{-3} s^{-1}] is the nucleation rate (i.e. the creation rate of seed particles) which is calculated for pure carbon chain molecules according to Gail et al. (1984). $\chi^{\rm net}$ [cm/s] is the net growth velocity of already existing dust surfaces by the accretion and thermal evaporation of carbon and hydrocarbon molecules. The functional dependencies of these quantities are

$$J_\star = J_\star(T_{\rm g}, n_k) \tag{9}$$

$$\chi^{\rm net} = \chi^{\rm net}(T_{\rm g}, T_{\rm d}, n_k) \tag{10}$$

$$n_k = n_k(\rho, T_{\rm g}, \epsilon_{\rm C}). \tag{11}$$

The various particle densities n_k entering into this description are calculated by assuming chemical equilibrium in the gas phase among H, H_2, C, O, CO, H_2O, C_2, C_3, CH, C_2H, C_2H_2, CH_4 according to the local mass density ρ, the local gas temperature $T_{\rm g}$, and the local carbon element abundance $\epsilon_{\rm C}$ in the gas phase. The latter obeys the following conservation law

$$\epsilon_{\rm C} + \frac{1.427\,{\rm amu}}{V_0} L_3 = \epsilon_{\rm C}^0 = {\rm const.} \tag{12}$$

$V_0 = 8.78\times10^{-24}$ cm^3 is the monomer volume of graphite and 1.427 amu the conversion factor between mass density ρ and hydrogen nuclei density $n_{\langle {\rm H}\rangle}$ for solar abundances. All other element abundances than carbon are assumed to have solar values. We take the oxygen abundance $\epsilon_{\rm O} = 10^{8.87-12}$ from (Noels & Grevesse 1993) and consider the carbon-to-oxygen ratio C/O = $\epsilon_{\rm C}^0/\epsilon_{\rm O}$ as a free parameter.

Dust evaporation is only included in terms of negative $\chi^{\rm net}$ in case of under-saturation. Negative particle fluxes in size space through the lower integration boundary at V_ℓ are neglected. For more details, see Gail & Sedlmayr (1988), Gauger et al. (1990) and Dominik et al. (1993).

2.4. Radiative transfer

Radiative transfer in dusty winds is a complicated problem. The optical depths are typically of the order of unity and the opaque regions can be confined into shells or clouds which move in an otherwise transparent medium. The opaque dust configurations scatter, re-emit and cast shadows, thereby illuminating the optically thin regions in between in complicated ways. Finding an efficient radiative transfer method to resolve these problems is the key to develop multi-dimensional models of dust-driven winds.

The absorption and thermal re-emission of radiation by dust grains leads to a very fast relaxation of the internal dust temperature to the local radiation field with cooling timescales of the order of milliseconds for small amorphous carbon grains (Woitke et al. 1999). This fast relaxation introduces a stiff coupling between hydrodynamics and radiative transfer. Any explicit scheme that is based on formal solutions of the radiative transfer problem (e.g. short characteristics method) has the disadvantage to slow down the computational timestep (typically

a few 10^4 s) to this radiative cooling timescale, which is not acceptable.

We therefore seek a numerical method that is capable to solve the continuum radiative transfer problem under the auxiliary condition that the dust component is in radiative equilibrium

$$\int \kappa_{\rm abs}^{\rm dust} J_\nu \,{\rm d}\nu = \int \kappa_{\rm abs}^{\rm dust} B_\nu(T_{\rm d}) \,{\rm d}\nu, \tag{13}$$

which de-stiffens the physical problem by the elimination of the shortest characteristic timescale via assuming a quasi-equilibrium. $\kappa_{\rm abs}^{\rm dust}$ is the dust absorption coefficient, $J_\nu(\boldsymbol{r}) = \frac{1}{4\pi}\int I_\nu(\boldsymbol{r},\boldsymbol{n})\,{\rm d}^2n$ the mean spectral intensity and B_ν the Planck function. In 2D or 3D, state-of-the-art Monte Carlo methods can do this job with the same accuracy as ray-based methods at a similar level of computational costs (e.g. Pascucci et al. 2004).

We have therefore developed a new software module for the FLASH-code which solves the LTE continuum radiative transfer with radiative equilibrium in spherical coordinates by a Monte Carlo (MC) method. According to our knowledge, this is actually the first report of such an approach in multi-dimensional fluid dynamics.

We have implemented the MC method of Niccolini et al. (2003) which solves the frequency-dependent radiative transfer problem with angle-dependent scattering. However, for this paper, we will only consider the grey case with isotropic scattering and simple frequency-averaged opacities, because we want to validate our new implementation by comparing the results of 1D spherically symmetric winds to former publications, where these opacities have been used (Fleischer et al. 1995; Höfner et al. 1995):

$$\widehat{\kappa}_{\rm ext} = \widehat{\kappa}_{\rm gas}^{\rm ext} + \widehat{\kappa}_{\rm dust}^{\rm ext} \tag{14}$$

$$\widehat{\kappa}_{\rm gas}^{\rm ext} = 2\times10^{-4}\,{\rm cm^2\,g^{-1}} \tag{15}$$

$$\widehat{\kappa}_{\rm dust}^{\rm ext} = \frac{3}{4}Q'(T_{\rm d})\,L_3 \quad \text{with } Q'(T_{\rm d}) = 5.9\,{\rm cm^{-1}}\left(\frac{T_{\rm d}}{\rm K}\right). \tag{16}$$

The constant gas opacity is taken from Bowen (1988) and the Rosseland mean extinction efficiency over particle radius $Q' = \langle\, Q_{\rm ext}(a,\lambda)/a \,\rangle_{\rm Ross}$ for small amorphous carbon grains from Gail & Sedlmayr (1985). Using Rosseland mean opacities yields the correct radiation pressure in optically thick winds. However, in optically thin winds, the radiation flux is not reddened with increasing distance and the radiation pressure will be hence underestimated for amorphous carbon.

Due to the extreme temperature-dependence of the nucleation and dust evaporation process, the noise level in the temperature determination should be as small as ±1 K (see results in Sect. 3.1.1). The statistical error in our MC method is determined by the number of crossing events of photon packages through a cell under consideration. Therefore, in order to achieve the required accuracy, one has to shoot many photon packages *and* one cannot use too small computational cells.

This condition practically prevents a solution of the radiative transfer problem on the partly very highly resolved AMR hydro-grid. Instead, a comparably coarse regular grid (equally spaced in log r and θ) is used for the radiative transfer calculations. A gas and dust mass conserving scheme has been implemented, based on cell volume overlaps, to map the $\{\rho, L_3\}(\boldsymbol{r})$ AMR hydro-data on this transfer grid. Next, the opacities are calculated and the Monte Carlo experiment is carried out, which results in the mean intensity structure $J(\boldsymbol{r}) = \frac{\sigma}{\pi}T_{\rm rad}^4(\boldsymbol{r})$. This data is finally interpolated back onto the hydro grid, using a 2D piecewise linear interpolation scheme. The whole procedure is treated as additional source term in the frame of the operator splitting method of the hydro solver.

In order to achieve the required temperature accuracy of ±1 K, the computational cost for one radiative transfer call is quite remarkable: about 40 s on one processor for a 200 − grid (1D) and about 120 s on 64 processors for a (120 × 80) − grid (2D). We are therefore forced to call the MC radiative transfer routine less frequently than at every hydro timestep.

Instead, we have developed an extrapolation scheme that allows us to call the radiative transfer routine only at about every 3rd to 100th hydro timestep. The basic idea for this extrapolation in time is to interpolate in optical depth space. For this purpose only, we calculate at every hydro-timestep the spherical optical depths (see Lucy 1971)

$$\tau_{\rm L}(r,\theta,t) = \int_r^{R_{\rm out}} \kappa_{\rm ext}(r',\theta,t)\left(\frac{R_\star^0}{r'}\right)^2 {\rm d}r'. \tag{17}$$

A parallel algorithm to compute these spherical optical depths for the stratification of the extended stellar atmosphere as given on the AMR hydro-grid with volume decomposition has been implemented, similar to the numerical method of Rijkhorst et al. (2005). $R_{\rm out}$ is the outer boundary of the model domain and $R_\star^0$ the stellar radius of the initial model (see Sect. 2.6). Given the last radiative transfer results $T_{\rm ref}(\boldsymbol{r}) = T_{\rm rad}(\boldsymbol{r}, t_{\rm ref})$ at reference time $t_{\rm ref}$ with reference optical depths $\tau_{\rm ref}(\boldsymbol{r}) = \tau_{\rm L}(\boldsymbol{r}, t_{\rm ref})$, the actual radiation temperatures are calculated as

$$\begin{aligned} T_{\rm rad}^4(\boldsymbol{r},t) &= T_{\rm ref}^4(\boldsymbol{r}) + a_{\rm cor}(\boldsymbol{r})\Big(t - t_{\rm ref}\Big) \\ &\quad + b_{\rm cor}(\boldsymbol{r})\Big(\tau_{\rm L}(\boldsymbol{r},t) - \tau_{\rm ref}(\boldsymbol{r})\Big), \end{aligned} \tag{18}$$

where $a_{\rm cor}$ and $b_{\rm cor}$ are local fit coefficients which are updated after every radiative transfer call. $b_{\rm cor}(\boldsymbol{r}) = \left.\frac{\partial T_{\rm rad}^4}{\partial \tau_{\rm L}}\right|_{\theta,t_{\rm ref}}(r)$ is the local dependence of $T_{\rm rad}^4$ on $\tau_{\rm L}$, which expresses typical back-warming effects. These effects can occur as fast as hydrodynamical changes, for instance if an opaque dust cloud enters a computational cell. $b_{\rm cor}$ is calculated by linear regression of the local $\{T_{\rm rad}^4, \tau_{\rm L}\}$ data points along the radial direction.

$a_{\rm cor}$ expresses the net change caused by all other radiative transfer effects, e.g. by the passing of a dust cloud sideways of a considered cell or by the changing shadow of a growing dust cloud between the star and the cell. These changes are usually caused by the more distant opacity configurations and hence occur on much longer timescales. After having fixed $b_{\rm cor}$, the second fit coefficient $a_{\rm cor}$ is calculated from inversion of Eq. (18), such that the extrapolation from the old to the new radiative transfer results would have been perfect.

The time interval $\Delta t_{\rm MC}$, after which the next proper MC radiative transfer must be calculated and the fit coefficients $a_{\rm cor}$ and $b_{\rm cor}$ are renewed, is controlled by the condition that the difference between the extrapolated $T_{\rm rad}$-values and the newly calculated $T_{\rm ref}$ MC results (measured by the 4-norm) must be smaller than $2\times\Delta_{\rm MC}T$, where $\Delta_{\rm MC}T \approx 1$ K is the Monte Carlo noise in the temperature determination.

We note that Eq. (18) allows for an exact treatment of the following two limiting cases

$$\begin{aligned} &T_{\rm ref}^4 = \frac{1}{2}\,T_{\rm eff}^4, \quad a_{\rm cor}=0, \quad b_{\rm cor}=\frac{3}{4}\,T_{\rm eff}^4, \quad \tau_{\rm ref}=0 \\ &\qquad \Rightarrow \text{ spherical diffusion approximation} \\ &\qquad\quad \text{(Eddington approximation)} \\ &T_{\rm ref}^4 = W(r)\,T_\star^4,\ a_{\rm cor}=0,\ b_{\rm cor}=\frac{3}{4}\,T_\star^4\left(\frac{R_\star}{R_\star^0}\right)^2,\ \tau_{\rm ref}=0 \\ &\qquad \Rightarrow \text{ spherical two-stream approximation} \\ &\qquad\quad \text{(Lucy's approximation),} \end{aligned} \tag{19}$$

where $W(r) = \frac{1}{2}\left[1-\left(1-\frac{R_\star^2}{r^2}\right)^{1/2}\right]$ is the radial dilution factor (see Lucy 1971). By fixing $T_{\rm ref}$, $a_{\rm cor}$ and $b_{\rm cor}$ in this way, or by keeping them updated according to the actual values of the stellar radius $R_\star(t)$ and stellar temperature $T_\star(t)$, respectively, one can run quick test models without involving the expensive MC radiative transfer routine. These simplifications, however, are only possible for spherically symmetric 1D models. 2D models require the proper inclusion of the MC radiative transfer.

Equation (18) is hence a reasonable approximation with the ability to self-adapt to certain limiting cases if the MC results indicate so. In general, it will only be valid in a local sense for a limited time span after a last proper solution of the radiative transfer problem. The extrapolated radiative transfer results are always time-resolved because they depend on the actual spherical optical depths.

Regarding the MC radiative transfer routine itself, scattering and thermal re-emission are numerically treated in different ways (Niccolini et al. 2003). In grey radiative transfer, however, isotropic scattering and thermal re-emission in radiative equilibrium are physically indistinguishable, so we can treat the albedo γ as a free parameter. Best performance, i.e. lowest noise at given computational time consumption, is achieved with $\gamma = 0.9$.

Another troublesome point is the $T_{\rm d}$-dependence of $\widehat{\kappa}_{\rm dust}^{\rm ext}$ which makes necessary an iterative procedure between opacity and radiative transfer calculations. We solve this problem by calling the MC routine only once (if it is foreseen for this timestep) and then using Eq. (18) in the subsequent iterations. After typically 1−5 iterations, this procedure converges (opacity calculation – optical depths calculation – $T_{\rm rad}$ recalculation). Only if it does not converge (which happens very seldom), more MC radiative transfer calls within this iteration loop are required.

2.5. Boundary conditions

Finding suitable boundary conditions for the multi-dimensional stellar wind problem in Eulerian coordinates (fixed volume) is not trivial. The main difficulty arises from the mass loss through the outer boundary which, on average, should be compensated for by a mass inflow at the inner boundary. The FLASH-code uses 4 layers of guard cells to describe boundary conditions. On these guard cells, all variables (ρ, $\boldsymbol{v}$, e, L_j) must be prescribed at every computational time step.

2.5.1. Inner boundary condition

The basic idea of our permeable inner boundary is to fix the gas pressure at the inner boundary. If matter is removed from the regions close to the inner boundary, e.g. blown away by radiation pressure, a pressure gradient across the inner boundary develops which causes the desired mass resupply from below.

In order to quantify this idea, we visit Eqs. (1) and (2) in the spherically symmetric stationary case, where they can be combined into the so-called wind equation

$$v_r\frac{\partial v_r}{\partial r}\left(1-\frac{c_T^2}{v_r^2}\right) - \frac{2c_T^2}{r} + \frac{\partial c_T^2}{\partial r} = a_{\rm rad} - a_{\rm grav}. \tag{20}$$

$c_T = \sqrt{p/\rho}$ is the isothermal sound speed. Assuming $v_r \ll c_T$ (subsonic limit), Eq. (20) becomes

$$-\frac{1}{v_r}\frac{\partial v_r}{\partial r} - \frac{2}{r} + \frac{1}{c_T^2}\frac{\partial c_T^2}{\partial r} = \frac{a_{\rm rad}-a_{\rm grav}}{c_T^2}. \tag{21}$$

By means of $\rho\, v_r r^2 = $ const. (the stationary case of Eq. (1)) one can show that the l.h.s. of Eq. (21) equals $\frac{\partial}{\partial r}\ln(\rho\, c_T^2)$, resulting in the integral

$$\ln(\rho\, c_T^2)\Big|_r = \ln(\rho\, c_T^2)\Big|_{r_0} + \int_r^{r_0} \frac{a_{\rm rad}-a_{\rm grav}}{c_T^2}\,{\rm d}r, \tag{22}$$

which shows that stationary flows in the subsonic limit in fact obey the hydrostatic condition. We use Eq. (22) to describe our inner boundary condition. We numerically evaluate the integral in (Eq. (22)) from an arbitrary point r on the guard cells to the first valid cell within the model volume r_0 by assuming that the gas temperature $T_{\rm g}$ can be linearly extrapolated backward from the first two valid cells in the radial direction.

One way to fix the gas pressure at the inner boundary would be $(\rho\, c_T^2)\big|_{r_0} = p(r_0, t=0)$. However, this simple idea leads to the problem that a sudden increase of the temperature level close to the inner boundary (e.g. due to a dust shell formation event) leads to a likewise sudden increase of the gas pressure level, which can result in a *positive* pressure gradient across the inner boundary, causing a vivid *infall* (negative velocities) through the inner boundary. According to our experience, it is better to fix the gas density at the inner boundary by

$$(\rho\, c_T^2)\Big|_{r_0} = \rho(r_0, t=0)\; c_T^2(r_0, t), \tag{23}$$

which leads to a more regular increase of the pressure level around the inner boundary (also on the guard cells) in case of a sudden irradiation from the outside. A positive temperature offset lowers $|\frac{\partial \ln p}{\partial r}|$, i.e. it causes a modest *outward acceleration* of the gas in case of a sudden irradiation from the outside, which seems more natural regarding a star to be characterised by an equilibrium between gravity and pressure forces.

Once having solved Eq. (22) for ρ, the radial velocity on the guard cells v_r is calculated from $\rho\, v_r r^2 = $ const., the internal energy e is calculated from ρ and $T_{\rm g}$ via the equation of state, and the guard cells at the inner boundary are assumed to be dust-free $L_j(r<r_0)=0$.

Since we do not consider stellar pulsation in this paper, a constant stellar luminosity $L_\star$ is assumed as inner boundary condition of the radiative transfer problem.

2.5.2. Outer boundary condition

For the outer boundary condition, a standard outflow condition (zero-gradient, i.e. a direct copy from the last valid cell designated by the subscript 0) is applied to the variables $\boldsymbol{v}$, $T_{\rm g}$ and L_j. The gas pressure is extrapolated in such a way that

the gradient $\frac{\partial p}{\partial r}$ compensates gravity and radiative acceleration (force-free):

$$\ln\, p\Big|_r = \ln\, p_0 + \frac{1}{c_{T_0}^2}\left(GM_{r_0} - \frac{\widehat{\kappa}_{\rm ext} L_\star}{4\pi\, c}\right)\left(\frac{1}{r_0} - \frac{1}{r}\right). \quad (24)$$

Equation (24) can be deduced from Eq. (22) under the assumption that M_r, c_T and $\widehat{\kappa}_{\rm ext}$ are constant on the guard cells. Mass density ρ and internal energy e are finally calculated from p and $T_{\rm g}$, using the equation of state.

2.5.3. Angular boundary conditions

In case of a 2D model, the guard cells at $\theta < 0$ and $\theta > \pi$ are filled by a standard reflecting boundary condition which assures $v_\theta(r, \theta = 0, t) = v_\theta(r, \theta = \pi, t) = 0$.

2.6. Initial condition

The dynamical simulations are started from a dust-free static stellar atmosphere as initial condition. In the static (and hence spherically symmetric) case, the Poisson equation, the equation of motion and the definition of the spherical optical depth form a system of ordinary differential equations

$$\frac{{\rm d}M_r}{{\rm d}r} = 4\pi r^2 \rho \quad (25)$$

$$\frac{{\rm d}p}{{\rm d}r} = \rho\left(\frac{\widehat{\kappa}_{\rm ext} L_\star}{4\pi r^2 c} - \frac{GM_r}{r^2}\right) \quad (26)$$

$$\frac{{\rm d}\tau_{\rm L}}{{\rm d}r} = -\rho\,\widehat{\kappa}_{\rm ext}\left(\frac{R_\star^0}{r}\right)^2 \quad (27)$$

which is completed by the equation of state $\rho = \rho(p, T_{\rm g})$, the gas opacity $\widehat{\kappa}_{\rm ext} = \widehat{\kappa}_{\rm gas}^{\rm ext}(\rho, T_{\rm g})$ and an analytic formula of the temperature as function of spherical optical depth $T_{\rm g} = T_{\rm g}(r, \tau_{\rm L})$. This formula represents the solution of the radiative transfer problem in radiative equilibrium.

Starting with an initial guess of this dependency, Eqs. (25) to (27) can be solved by a standard ODE solver with the outer boundary condition

$$\tau_{\rm L}(R_{\rm out}) = 0 \quad (28)$$

and two conditions at the stellar radius

$$M_r(R_\star^0) = M_\star \quad (29)$$

$$T_{\rm g}(R_\star^0) = T_{\rm eff}, \quad (30)$$

where the initial stellar radius $R_\star^0$ is given by the Stefan-Boltzmann law $L_\star = 4\pi R_\star^{0\,2} \sigma T_{\rm eff}^4$.

Having obtained this solution, the MC radiative transfer routine is called for given gas density distribution $\rho(r)$ which provides new $\{r, T_{\rm g}, \tau_{\rm L}\}$ data points, from which an updated version of the temperature formula (piecewise linear interpolation) is calculated. The procedure needs about 3−10 iterations to converge.

The physical parameters of the complete static stellar atmosphere problem are hence the stellar luminosity $L_\star$, the effective temperature $T_{\rm eff}$ and the stellar mass $M_\star$. The static stratification is calculated during the initialisation phase of the FLASH-hydrocode. The solution is then mapped onto the initial FLASH-grid, again using a piecewise linear interpolation scheme in r.

2.7. Timestep control

The computational timestep of the dust radiation hydrodynamics code is limited by two criteria. First, 0.8× the Courant-Friedrich-Levy timestep, given by the minimum of the sound wave travel time through any computational cell, and second, a temperature limiter. The latter limits the maximum change of $T_{\rm rad}$ during one computational timestep to some given value. We choose this value to be 5 K, which seems necessary for the simulation of dust formation and in fact stabilises the results.

2.8. Model domain and grid resolution

As radial model domain, the interval $r/R_\star^0 \in [0.9, 10]$ is considered. In case of a 2D-model, the full angular range $\theta \in [0, \pi]$ is considered. The choice of the location of the inner boundary results typically in truly subsonic velocity variations and diffusive radiative transfer conditions ($\tau_{\rm L} \approx 5$) at the inner boundary. The outer boundary is located far outside the dust formation and wind acceleration zone. We have checked that a larger choice than $10\,R_\star^0$ has only minor influence on the resulting wind quantities like e.g. the mass loss rate.

We start with a basic grid resolution (refinement level 1) of $[r \times \theta] = 96 \times 64$ cells. Based on second derivative criteria, the grid will be refined during the simulation to maximum level 5. Each refinement step increases the local resolution block-wise by a factor of two in each spatial dimension, such that the maximum resolution (if the grid needs to be fully refined) is 1536×1024.

2.9. Computational limitations

The implementation of the physical and chemical processes (source terms) in the frame of the FLASH-solver is independent of spatial dimension and applied coordinate system, such that now 1D/2D/3D FLASH simulations with Cartesian or curvilinear coordinates are principally possible. We find it, however, most convenient, if not even mandatory, to formulate the boundary conditions with spherical coordinates. Furthermore, the Monte Carlo radiative transfer code does currently only allow for 1D and 2D models with spherical coordinates.

A complete high-resolution 1D model (60 years of simulation) requires about 5×10^5 CPU s, a complete 2D high-resolution model about 5×10^7 CPU s on ASTER, which is an SGI Altix 3700 system consisting of 416 processors (Intel Itanium 2, 1.3 GHz). We have typically used 8 processors for a 1D model (16 h user time) and 64 processors for a 2D model (9 days). Hence, even with the present power of modern parallel super-computers, 3D simulations with Monte Carlo radiative transfer are simply too expensive for the required accuracy (see Sect. 3.1.1). Thus, for practical purposes, only 1D (spherically symmetric) and 2D (axisymmetric) simulations can be run with the present code.

3. Results

The description of our results is separated into two parts. First, we compare our results for spherically symmetric (1D) dust-driven winds with other published works in Sect. 3.1, intending to validate our new numerical implementation. In Sect. 3.2, the new axisymmetric (2D) models will be presented and discussed.

Table 1. Results of 1D spherically symmetric models for C/O increase (see text). Constant parameters: $M_\star = 1\,M_\odot$ and $L_\star = 10^4 L_\odot$.

$T_{\rm eff}$ [K]	C/O	$\dot{M}\ \left[\frac{M_\odot}{\rm yr}\right]$	v_∞ [km s^{-1}]	$\rho_{\rm d}/\rho_{\rm g}$	Remarks
2400	1.6	≈3(−7)	<2	≈8(−4)	breeze
2400	1.65	4.6(−7)	4.1	8.1(−4)	stationary
2400	1.7	6.3(−7)	6.1	8.6(−4)	stationary
2400	1.75	1.0(−5)	24.6	2.7(−3)	P = 790 d
2400	1.8	1.1(−5)	25.2	2.7(−3)	P = 790 d
2400	1.9	9.9(−6)	26.8	2.9(−3)	irregular
2500	1.8	≈1(−7)	<2	≈1(−3)	breeze
2500	1.85	2.3(−7)	5.1	8.1(−4)	stationary
2500	1.9	3.1(−7)	6.8	8.6(−4)	stationary
2500	1.95	4.0(−7)	8.7	9.5(−4)	stationary
2500	2.0	5.5(−7)	11.5	1.3(−3)	stationary[(1)]
2500	2.05	6.9(−6)	27.5	2.7(−3)	P = 660 d
2500	2.1	6.2(−6)	30.7	3.1(−3)	irregular
2500	2.2	7.9(−6)	31.7	3.2(−3)	irregular
2600	2.0	≈3(−8)	<2	≈9(−4)	breeze
2600	2.1	7.1(−8)	4.2	7.8(−4)	stationary
2600	2.2	1.2(−7)	7.2	8.6(−4)	stationary
2600	2.3	1.9(−7)	10.2	9.8(−4)	stationary
2600	2.4	3.8(−6)	32.0	3.3(−3)	irregular
2600	2.5	3.9(−6)	35.5	3.4(−3)	irregular

breeze: Subsonic solution with finite outer pressure for $r \to \infty$ (unphysical). In the numerical model, such solutions are characterised by a standing shock wave in the outer regions.

P = ...: Quasi-periodic solution. All global quantities like $\dot{M}(t)$ or $M_{\rm d}(t)$ show cyclic variations (see Fig. 3). The Fourier spectra are characterised by an outstanding peak at a certain period P [days]. Dust is produced at every cycle, but small cycle-to-cycle variations may exist.

irregular: Oscillatory solution with irregular dust shell production. No clear period. Sometimes period switches.

(1): Stationary solution with small oscillatory perturbations (very close to the bifurcation point).

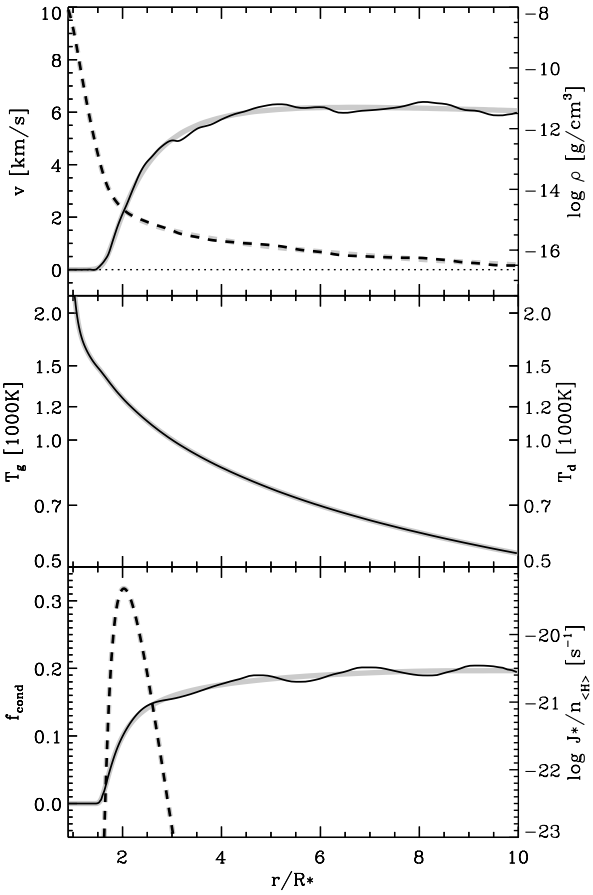

Fig. 1. Stationary 1D wind solution for $M_\star = 1\,M_\odot$, $L_\star = 10^4\ L_\odot$, $T_{\rm eff}$ = 2400 K and C/O = 1.7. The thin black lines show the velocity v (full), the mass density ρ (dashed), the dust and gas temperatures $T_{\rm d}$ and $T_{\rm g}$ (full – practically identical in this model), the degree of condensation $f_{\rm cond}$ (full) and the nucleation rate per hydrogen nucleus $J_\star/n_{\langle {\rm H}\rangle}$ (dashed). The underlying thick grey lines show the results for a comparison model, where the Monte Carlo radiative transfer code is not called anymore (see text). The difference between black and grey indicates the effect of the Monte Carlo radiative transfer noise ($\Delta T_{\rm MC} \approx 1$ K) on the solution.

3.1. 1D results: code validation

Fleischer et al. (1995) and Höfner et al. (1995) have published spherically symmetric (1D) models for time-dependent dust-driven winds of carbon stars with the same physical equations and assumptions (e.g. no pulsation) and parameters (e.g. opacities) as in our model, but using different numerical techniques. These results can hence be used to validate our new computational implementation. We will briefly summarise the basic results obtained by all three models, before we can discuss the differences.

After the start of a new simulation, the initially hydrostatic and dust-free stratification of the stellar atmosphere and the circumstellar environment undergoes some dramatic changes with strong shock waves in the outer regions. However, the model structure soon relaxes towards a new type of solution, which is found to be either a *stationary wind* or an *oscillating wind*.

3.1.1. Stationary winds

The stationary solutions are characterised by low mass loss rates $\dot{M}$, low outflow velocities v_∞ and low dust-to-gas ratios $\rho_{\rm d}/\rho_{\rm g}$ and occur for comparably small C/O ratios (see Table 1). Figure 1 shows an example for such a finally almost time-independent solution. The inner regions, from the bottom of the atmosphere to the start of the dust formation zone, are approximately in hydrostatic equilibrium. The density falls off exponentially here and the velocity is approximately zero. At some distance from the star (here at about $1.5\,R_\star$) the temperature becomes low enough for nucleation which triggers the process of dust formation. Radiation pressure on dust then accelerates the dust/gas mixture and drives it through the sonic point located at about $2\,R_\star$ in the depicted model. The wind region beyond that point is characterised by an almost constant outflow velocity and a $\rho \propto r^{-2}$ law. Due to the increasingly rapid outflow and the decreasing gas densities, the process of dust formation freezes in. For further details, see e.g. Gail & Sedlmayr (1987).

Note that the formation of dust remains incomplete. Only about 18% of the condensable carbon has actually condensed into solid particles in the depicted model (see $f_{\rm cond}$ in Fig. 1). The influence of the dust formation on the radiative transfer results is small. The model describes an optically thin, low-velocity, dust-driven stellar wind.

Due to the Monte Carlo noise in the temperature determination of our radiative transfer code (see Sect. 2.4), the relaxation towards a stationary wind is actually never complete. The slightly random radiative transfer results cause small temperature changes in the inner regions which create inward and outward travelling sound waves. The outward travelling

waves amplify in the large density gradient close to the star. This amplification of waves and the strong temperature dependence of the nucleation process result in noticeable variations of the fluid variables in the outer regions of order 5%, although the temperature noise $\Delta T_{\rm MC}$ is as small as 0.1% (not visible). This result leads us to the conclusion that an accuracy of the radiative transfer results of $\Delta T_{\rm MC} \approx 1$ K is actually required to model dust-driven winds, which makes the simulations very expensive. We have checked that a reduction of the Monte Carlo noise by a factor of two (by using four times more photon packages) reduces the amplitudes of the remaining disturbances by about a factor of two.

We can suppress the creation of new disturbances completely by not calling the radiative transfer routine anymore, thereby fixing $T_{\rm ref}$ and $b_{\rm cor}$ for ever and putting $a_{\rm cor} = 0$ (see Eq. (18))[1]. In that case, the stationary solution becomes completely smooth and freezes in for all times (see underlying grey model in Fig. 1). This freezing for arbitrary long times is possible, because our inner boundary condition compensates the mass loss through the outer boundary, in contrast to the Fleischer et al. (1995) and Höfner et al. (1995) models, where the model volume runs empty for very long times.

3.1.2. Oscillatory winds

Beyond some critical value for the stellar luminosity (Fleischer et al. 1995) or the C/O ratio (Höfner et al. 1995), the stationary wind solutions become unstable. This instability, called "exterior κ-mechanism", is caused by feedbacks of the dust formation process on the radiative transfer. After the formation of a new optically thick dust shell, the temperatures inside of this shell increase quickly due to *backwarming* (see $T_{\rm d}(r)$ in Fig. 2), which switches off the nucleation process and may even cause dust evaporation in the inner regions. The newly formed dust shell is hence truncated at its inner edge and driven outward, which reduces again its optical depth because of radial dilution. Consequently, the temperatures in the inner regions start to slowly decrease again, and a new cycle of dust formation may begin.

This mechanism, however, interferes with other hydrodynamical processes in the dust formation zone. The sudden acceleration of a newly formed dust shell creates two waves. The first wave, an outward travelling compression wave, steepens up into a shock wave, compresses the gas ahead of the outward moving shell and facilitates subsequent dust formation in the wake of this shock. The second wave, an inward travelling expansion wave, causes the dust formation zone to be re-filled with fresh matter from the star. The sudden increase of the temperatures in the stellar atmosphere creates a third wave, a pressure-driven expansion wave, which merges with the incoming expansion wave to create a new shock wave below the dust formation zone. These hydrodynamical disturbances affect the structure of the stellar atmosphere and may interfere with the stellar pulsation (disregarded in this paper). The characteristic timescale of the dust-induced κ-mechanism (usually longer than typical pulsational periods) may or may not coincide with the timescale of these hydrodynamical processes. A complicated time-dependent behaviour results in this way, which can be periodic, multi-periodic or completely irregular (see Fig. 3).

As a common result from all three simulations (this work; Fleischer et al. 1995; Höfner et al. 1995), the oscillatory solutions are characterised by higher mass loss rates $\langle \dot{M} \rangle$, higher outflow velocities $\langle v_\infty \rangle$ and higher dust-to-gas ratios $\langle \rho_{\rm d}/\rho_{\rm g} \rangle$ as compared to the stationary solutions (measured by temporal mean values at the outer boundary). The solutions describe optically thick winds of sometimes massively obscured central stars, e.g. infrared carbon stars.

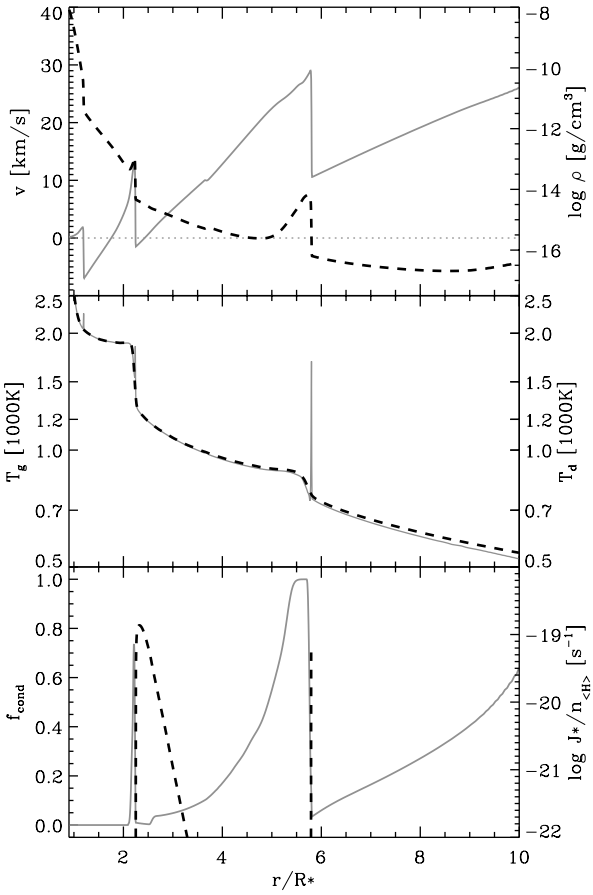

Fig. 2. Snap shot of an 1D oscillating wind solution for the same stellar parameters as in Fig. 1 but with slightly increased C/O = 1.75. In this plot, grey full lines refer to l.h.s. quantities and black dashed lines to r.h.s. quantities.

The effect of the Monte Carlo noise on the oscillatory wind solutions is more difficult to assess, because we cannot suppress it completely. The ongoing creation of small temperature disturbances by the MC noise in the stellar atmosphere prevents a complete relaxation to a truly periodic solution. Therefore, our solutions are always featured by small deviations from periodicity or are even irregular. This behaviour, however, was also found by Fleischer et al. (1995) and Höfner et al. (1995), who used deterministic radiative transfer methods. If we use the deterministic Lucy approximation for the radiative transfer (see Sect. 2.4), we can produce solutions for some parameter combinations which are sometimes closer to truly periodic, but the general behaviour of the solutions is very similar. Therefore, we conclude that the Monte Carlo noise is not a critical issue concerning the resulting type of wind solution.

3.1.3. Comparison to other 1D models

The general behaviour of our new FLASH simulations for dust-driven C-star winds in the special case of spherical symmetry resembles well the behaviour reported by Fleischer et al. (1995)

[1] This is not the same as fixing the temperature profile: τ-changes still cause $T_{\rm rad}$-changes.

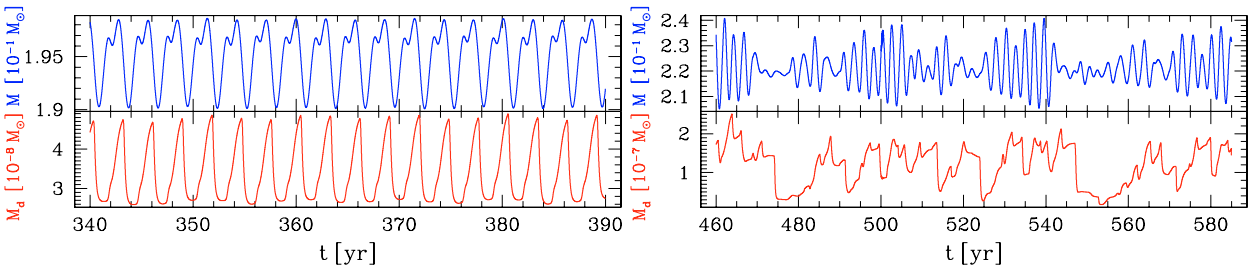

Fig. 3. Examples for "quasi-periodic" (l.h.s.: $T_{\rm eff}$ = 2500 K, C/O decrease to 1.6) and "irregular" (r.h.s.: $T_{\rm eff}$ = 2400 K, C/O decrease to 1.6) 1D oscillatory wind solutions. Depicted is the total gas + dust mass $M(t)$ (*upper row*) and the total dust mass $M_{\rm d}(t)$ (*lower row*) contained in the model volume. The change of $M(t)$ is mainly due to mass inflow and outflow through the inner boundary. The change of $M_{\rm d}(t)$ is due to dust formation and mass loss through the outer boundary. In the quasi-periodic model (l.h.s.), a new shell of dust is formed at every second oscillation cycle (double-periodic solution). Fourier analysis shows two sharp maximums at 1060 and 530 days. The basic period P = 530 days given in Table 1 refers to the oscillation of the stellar atmosphere. The irregular model (r.h.s.) shows the production of dust shells at almost unpredictable instants of time.

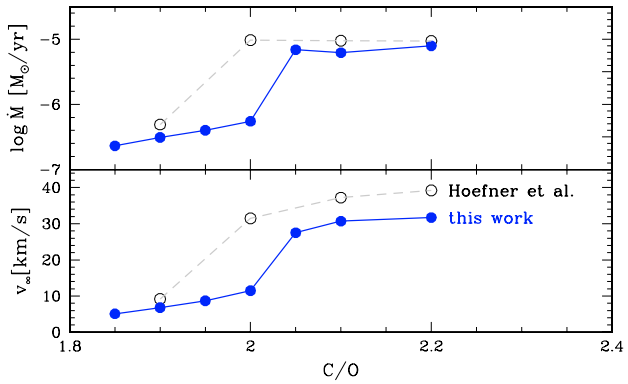

Fig. 4. Comparison of 1D results to Höfner et al. (1995) for $M_\star = 1\,M_\odot$, $L_\star = 10^4\,L_\odot$ and $T_{\rm eff}$ = 2500 K.

and Höfner et al. (1995), progressing from breezes → stationary winds → oscillatory solutions with increasing C/O. In a comparative study, Höfner et al. (1996) have argued for good general agreement between the two codes despite the different numerical techniques. Since Fleischer et al. (1995) have considered throughout higher stellar luminosities than in this paper, we will concentrate on the comparison to the Höfner et al. models in the following.

Figure 4 shows the differences of the calculated mean wind quantities to Höfner et al. (1995, see their Table 3). In summary, the Höfner et al. winds are a little stronger with slightly larger $\dot{M}$ and v_∞. One can also describe these differences in the following way. The "jump" from stationary → oscillatory solutions in our models occurs at a slightly larger critical C/O value as compared to the Höfner et al. models. The obtained periods of Höfner et al. show the same trend (increasing with increasing $T_{\rm eff}$) but are throughout shorter by a factor of about 1.5.

The slightly lower efficiency of the driving by dust in our work can already be explained by a tiny detail in the treatment of equilibrium chemistry. In contrast to Höfner et al. (1995), we have included the C_3 molecule which reaches high concentrations around ≈2000 K and thereby reduces the number density of C atoms and C_2H_2 molecules. This lowers the efficiency of the nucleation and growth of the carbon dust particles. According to our model, just ignoring the C_3 molecule results in higher $\dot{M}$ and v_∞ by a factor of about two in the stationary regime, which would put our results even above those of Höfner et al. in Fig. 4.

However, various other numerical details could also be the reason for the shown discrepancies. With regard to the very complex physical system under investigation, small numerical deviations can have big effects. In view of the different radiative transfer methods, the different implementation of the hydrodynamical equations with different numerical schemes (implicit/explicit) and, last but not least, the different inner boundary condition, the degree of agreement is actually quite remarkable.

3.1.4. The folding bifurcation

The results of our 1D simulations, as summarised in Table 1, have been obtained by a stepwise increase of C/O, giving the model sufficient time in between to relax to the respective equilibrated solution (about 50 yr).

However, if we stepwise *decrease* C/O again, we face a surprise (see Table 2). The model does not fall back toward the stationary solution at the critical C/O value for increase as observed before. Instead, it stays oscillatory until it finally falls back to a "breeze" at another, much lower critical C/O value for decrease. Apparently, once the transition to an oscillatory mode is made and the outer parts of the stellar atmosphere are swinging back and forth considerably, a more efficient mechanism of dust production can be sustained even with less fuel. This non-uniqueness for intermediate C/O values (hysteresis behaviour/folding bifurcation) is sketched in Fig. 5 and has not been reported so far.

3.1.5. Oscillating low-velocity solutions

The reason for the folding bifurcation sketched in Fig. 5 lies in an accumulation of small amounts of dust particles in the "metastable" region close to the star which is too hot for nucleation, but too cold for dust evaporation. In a stationary wind, this region remains completely dust-free because of the throughout positive radial velocities. However, in case of oscillations, some dust particles (which have been created farther out) periodically re-enter this region, where they temporarily stay and grow up to very big particles with radii as large as $\langle a \rangle = \left(\frac{3}{4\pi}\right)^{1/3} L_1/L_0 \approx 50\,\mu$m. The total surface of these few big grains remains so small, however, that an average molecule needs about $\tau_{\rm coll} = \left(v_{\rm th}(36\pi)^{1/3}\rho L_2\right)^{-1} \approx 100$ yr to collide with them. Hence, the degree of condensation and the dust opacity are practically frozen in and remain too small to cause a net outward acceleration $|a_{\rm rad}| \lesssim |a_{\rm grav}|$. However, $a_{\rm rad}$ is just large enough to change the pressure gradient in this quasi-static region, which leads to higher densities in the outer parts.

Table 2. Results of 1D spherically symmetric models for C/O decrease (see text). Constant parameters: $M_\star = 1\,M_\odot$ and $L_\star = 10^4\,L_\odot$.

$T_{\rm eff}$ [K]	C/O	$\dot{M}$ [$\frac{M_\odot}{\rm yr}$]	v_∞ [km s^{-1}]	$\rho_{\rm d}/\rho_{\rm g}$	Remarks
2400	1.7	1.1(−5)	23.7	2.5(−3)	$P = 790$ d
2400	1.6	9.8(−6)	19.0	1.8(−3)	irregular
2400	1.5	5.4(−6)	18.0	1.6(−3)	irregular
2400	1.4	1.1(−6)	3.4	7.8(−4)	osc. breeze
2400	1.3	3.0(−7)	0.4	8.9(−4)	osc. breeze
2500	2.0	7.2(−6)	30.0	3.0(−3)	irregular
2500	1.9	7.1(−6)	25.2	2.3(−3)	irregular
2500	1.8	4.8(−6)	21.0	1.9(−3)	irregular
2500	1.7	3.9(−6)	21.2	1.6(−3)	irregular
2500	1.6	3.4(−6)	20.7	1.6(−3)	$P = 530$ d$^{(2)}$
2500	1.5	5.8(−7)	2.8	3.7(−4)	osc. breeze
2600	2.3	4.6(−6)	31.3	2.9(−3)	irregular
2600	2.2	4.2(−6)	27.5	2.3(−3)	irregular
2600	2.1	2.8(−6)	26.3	2.1(−3)	irregular
2600	2.0	1.2(−6)	20.8	1.7(−3)	irregular
2600	1.8	1.7(−6)	20.9	1.7(−3)	$P = 630$ d$^{(2)}$
2600	1.7	2.5(−6)	19.4	1.4(−3)	$P = 620$ d$^{(2)}$
2600	1.6	1.6(−7)	1.1	9.3(−4)	osc. breeze

osc. breeze: Low-velocity solution (sometimes subsonic v_∞) with small oscillations and persistent dust inside the nucleation regime (see Fig. 6).

(2): Double-periodic: formation of a dust shell at every second oscillation cycle of the outer stellar atmosphere.

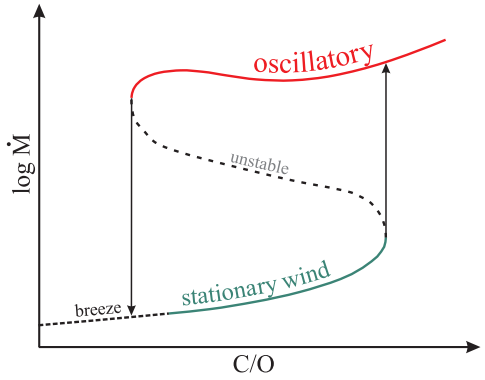

Fig. 5. Folding Bifurcation in modelling C-star winds.

This density levitation facilitates dust formation in the outer parts and leads to a persistent, oscillatory stellar outflow with low (sometimes subsonic) velocities and a smooth dust distribution, see Fig. 6. Winters et al. (2002) described similar low-velocity, almost quasi-static ("B-type") 1D wind solutions in a certain range of stellar parameters under the influence of a strong stellar pulsation as inner boundary condition. Here, we find the same type of wind solution even without stellar pulsation.

The question remains open whether or not such low-velocity outflows exist in reality. Jura et al. (2002) noted that the close-by semi-regular variable L_2 Pup (spectral type M5 IIIe−M6 IIIe) has in fact a very low-velocity outflow ($v_\infty \approx 1.9\,{\rm km\,s^{-1}}$). Based on continuum observations, Jura et al. (2002) estimated the mass-loss rate of L_2 Pup to be $\dot{M} \approx 3.5 \times 10^{-7}\,M_\odot$/yr, whereas based on molecular line observations, Winters et al. (2002) estimated $\dot{M} \approx 2 \times 10^{-9}\,M_\odot$/yr. Despite this large scatter, these wind properties seem to match the characteristics of the low-velocity outflows as found by Winters et al. (2002) and in this work. However, L_2 Pup is an oxygen-rich star with lower

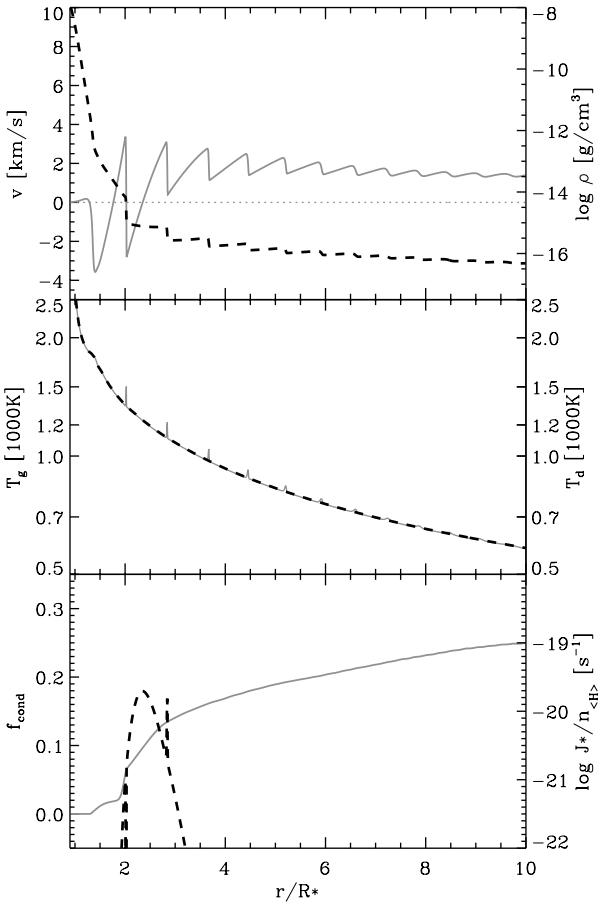

Fig. 6. Subsonic 1D solution with small oscillations for $M_\star = 1\,M_\odot$, $L_\star = 10^4\,L_\odot$, $T_{\rm eff} = 2600$ K obtained by *decreasing* C/O↘1.6 after about 1800 years of simulation. Note the small but non-zero degree of condensation inside the nucleation peak. For clarity, we have "frozen" this solution at later stages by not calling the MC radiative transfer routine anymore (see Fig. 1 and text).

luminosity, higher stellar mass and higher effective temperature than assumed in these models, so this link between observations and theoretical models is weak.

3.2. Results of the 2D models

The major aim of this work is to advance from 1D to 2D dust-driven wind models. This enables us, for the first time, to explore the effects of deviations from spherical symmetry on dust-driven winds in a consistent way[2]. Can these complicated physico-chemical systems, which have been proven to be unstable already in 1D models, keep their spherical symmetry, or – do instabilities lead to spontaneous symmetry breaking, structure formation and more complex flow patterns, for example turbulent mixing? The answer of the 2D simulations is quite unambiguous.

3.2.1. The Rayleigh-Taylor type instability

Already shortly after the start of a new simulation, the expanding dust shells experience Rayleigh-Taylor type instabilities at

[2] Freytag & Höfner (2003) have passively integrated the dust moment equations in first 3D simulations, without taking into account the important feedbacks of the dust on the acceleration and on the radiative transfer.

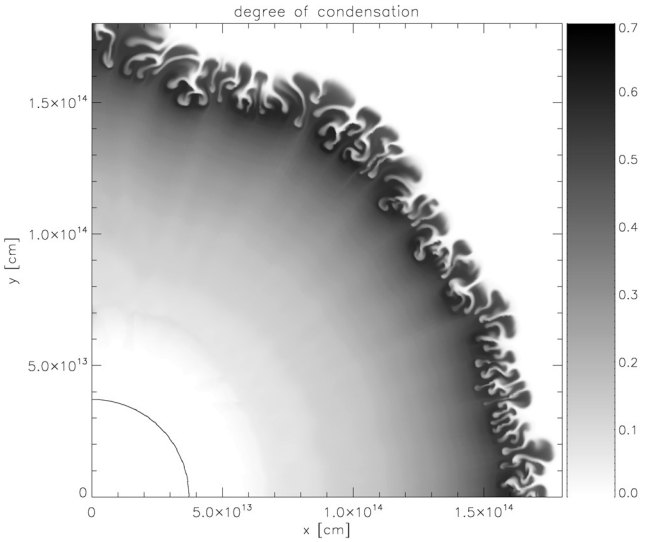

Fig. 7. Rayleigh-Taylor instabilities in an expanding dust shell shortly after the start ($t = 3.2$ yr) of a new axisymmetric (2D) simulation. Stellar parameters $M_\star = 1\,M_\odot$, $L_\star = 10^4\,L_\odot$, $T_{\rm eff} = 2500$ K and C/O = 1.9. The additional contour line for $T_{\rm rad} = 2500$ K indicates the size of the star.

their outer edges (see Fig. 7), which break the spherical symmetry spontaneously. This instability will be further analysed and discussed in a forthcoming paper (Woitke et al. 2006), but their nature is easy to understand. The dust containing gas, which has a larger opacity $\widehat{\kappa}_{\rm ext}$ and hence a higher potential energy $-GM_\star(1-\alpha)/r$ with $\alpha = \widehat{\kappa}_{\rm ext}L_\star/(4\pi cGM_\star)$ (see Eq. (6)), is accelerated into a dust-poor gas with lower opacity and hence lower potential energy. Thus, it is energetically favourable to exchange matter across the outer interface of a dust shell, which makes the fluid unstable.

According to the 2D simulations, a spontaneous mixing occurs in most cases at the outer edges of dust shells, where dust-rich fingers penetrate outward and more transparent dust-poor fingers penetrate inward with respect to the outward moving shell. The occurrence of Rayleigh-Taylor type instabilities is a persistent feature also in the more relaxed 2D models.

3.2.2. Description of 2D solutions

In the following, we will describe the qualitative behaviour of two relaxed 2D models with emphasis on the main new features caused by dropping the assumption of spherical symmetry[3].

The first high-resolution 2D model has been calculated for parameters $M_\star = 1\,M_\odot$, $L_\star = 10^4\,L_\odot$, $T_{\rm eff} = 2500$ K and C/O = 1.9. This set of parameters results in an optically thin stationary wind with only little θ-variations. The radial structures (cuts along constant θ) resembles well the respective 1D model structure (see Sect. 3.1.1).

The second high-resolution 2D model has been calculated for the same stellar parameters, but now with C/O = 2.2, a parameter combination which resulted in an optically thick wind with irregular oscillating behaviour in 1D (see Table 1). Figure 8 shows some details of this 2D model after 46.5 yr of simulation, after which the respective 1D model is sufficiently relaxed.

The most striking new feature is that the dust "shells" are not complete but only occupy a certain fraction of the total solid angle. These dust "arcs", sometimes also smaller "caps" originate from the dust formation zone which is mainly radially oscillating according to the exterior κ-mechanism known from the 1D models (see Sect. 3.1.2). However, these oscillation often become out-of-phase concerning north-polar, equatorial and south-polar regions, etc., in the final relaxed state. Consequently, dust forms from time to time in restricted regions above the stellar surface. Only in those cases where the complete dust formation zone around the star performs a concerted radial oscillation, a complete radial dust shell is produced. In all other cases, the production of limited dust arcs is more typical.

In fact, the different polar and equatorial regions seem to perform more or less their own independent oscillations, since they are only weakly coupled to each other via tangential velocities and radiative transfer feedbacks. Considering the often slightly chaotic behaviour of the dust formation zone in the 1D models (weak chaos), it's clear that small disturbances (e.g. introduced by the Monte Carlo noise or by the Rayleigh-Taylor instability) may cause completely different trajectories after sufficiently long times.

There is, however, one mechanism that tends to equilibrate the phases of the oscillations and to reinstall spherical symmetry, namely the radiative backwarming, which interrupts the dust production inside a forming shell (see Sect. 3.1.2). However, this backwarming is not as simple as in 1D geometry. It has only a limited reach and cannot trigger the dust formation at the opposite side of the star. We believe that this is the reason why the typical angular extent of the dust arcs in the model is about one forth to one half of the total solid angle: An arc of such an angular extension produces locally almost as much backwarming as a complete radial shell.

Figure 9 shows further details of the calculated temperature structures. The radiative transfer through the clumpy dust arcs causes complex temperature patterns with backwarming, sidewarming and shadow formation. The consequence is that the next dust formation episode will occur preferentially in those regions close to the star which are now not so much affected by the radiative backwarming.

Once a dust arc has formed, it is accelerated outward by radiation pressure. This outward motion causes not only a radial displacement and dilution, but also a tangential expansion because of the decreasing ambient pressure. Supersonic tangential velocities result in this way (see lower r.h.s. part of Fig. 8) which increase the angular size of the arcs. At the side edges of the dust arcs, the matter stays behind and continues to form more dust which leads to an apparent inward bending and extension of the arcs. Concerning the smaller dust caps, the expansion motion resembles the behaviour of mushroom clouds: tangential expansion at the top and counter-rotating vortices in the wake with Kelvin-Helmholtz instabilities.

The occurrence of negative (infall) velocities underneath and within the dust formation zone is a typical feature in all oscillating wind models, not only in 1D but also in 2D. However, in the 2D case, dust-poor gas may fall back toward the star at the same time as dust-rich gas is accelerated outward. In fact, these infall motions occur typically just between the outward moving arcs and clouds. Since the infalling gas is compressed by the ambient pressure, the infalling dust-poor regions are usually much smaller than the outward moving dust-rich structures.

[3] Unfortunately, the 2D models are so expensive (see Sect. 2.9) that only two complete high-resolution 2D simulations are available up to now, supplemented by a number of additional low-resolution simulations.

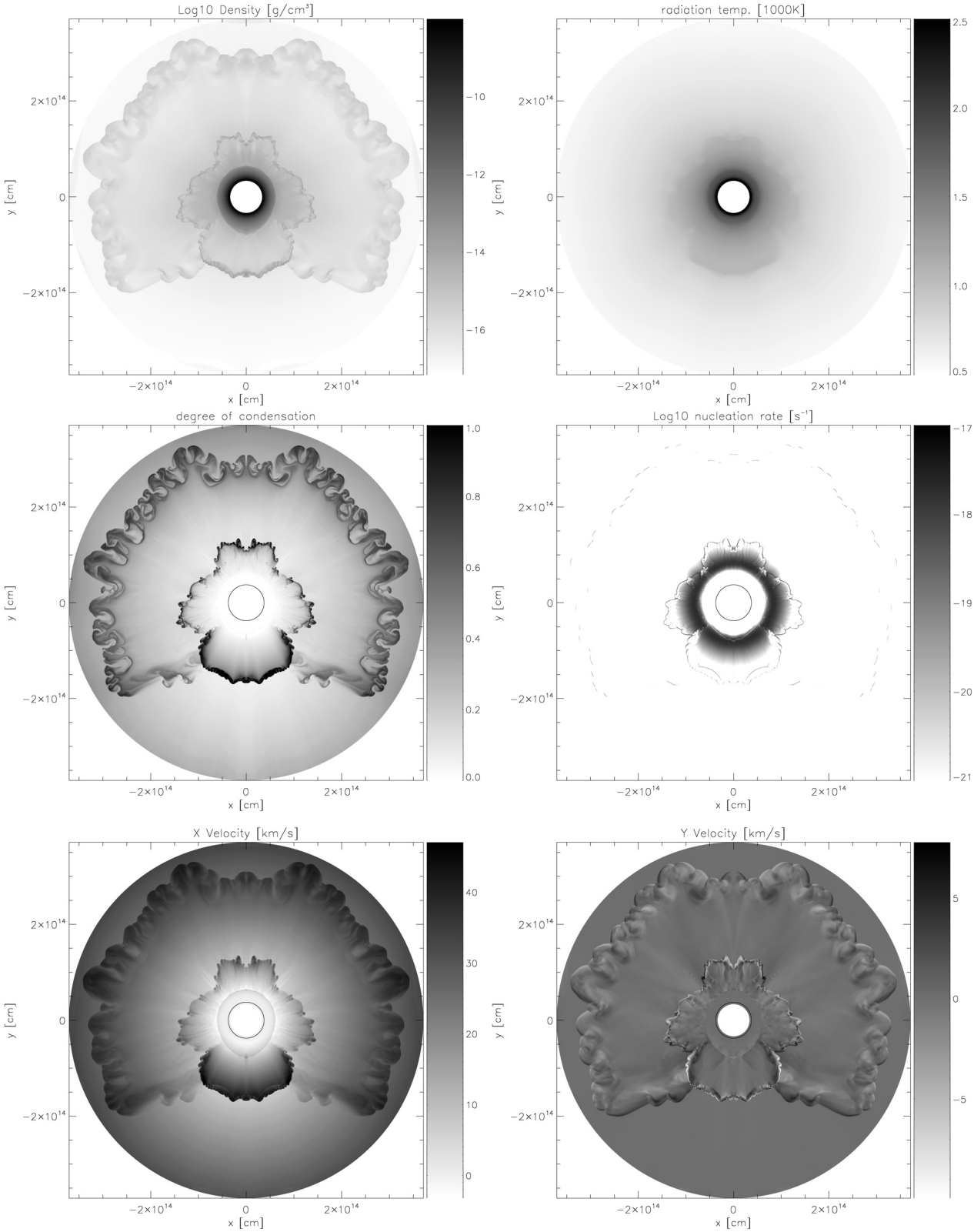

Fig. 8. Snap-shots after 46.5 years of simulation from an axisymmetric (2D) model with parameters $M_\star = 1\,M_\odot$, $L_\star = 10^4\,L_\odot$, $T_{\rm eff} = 2500$ K and C/O = 2.2, showing the following quantities as grey-scale plots: *first row*: mass density log ρ and radiation temperature $T_{\rm rad}$, *second row*: degree of condensation $f_{\rm cond}$ and nucleation rate per hydrogen nucleus $\log(J_\star/n_{\langle \rm H \rangle})$, *last row*: radial velocity v_r and tangential velocity v_θ (white indicates a motion towards the north pole and black towards the south pole). The additional black contour line for $T_{\rm rad} = 2500$ K indicates the size of the star. Central blank regions are not included in the model.

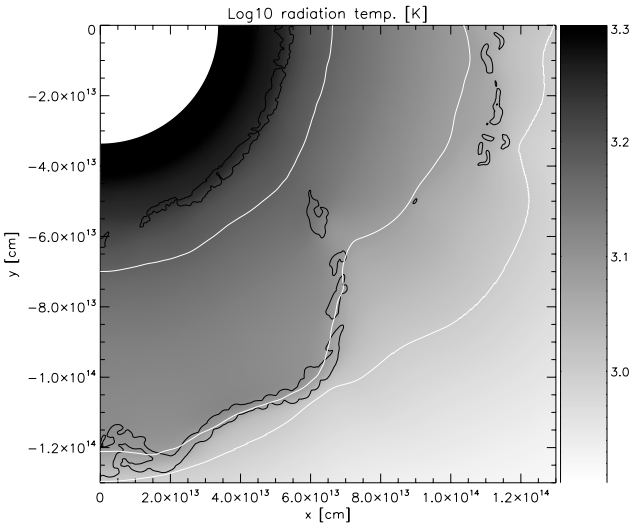

Fig. 9. Details of the radiation temperature structure in the 2D model shown in Fig. 8 (same timestep) with overplotted white contour lines for $T_{\rm rad}$ = 1000 K, 1200 K and 1500 K. The additional black contour line for $\kappa_{\rm ext} = 5{\times}10^{-14}$ cm^{-1} encircles the optically thick dust structures. Note the backwarming of the dust arc at the bottom and the formation of shadows behind the opaque regions.

Table 3. Comparison of calculated wind quantities between 1D and 2D models for $M_\star$ = 1 $M_\odot$, $L_\star$ = 10^4 $L_\odot$, $T_{\rm eff}$ = 2500 K and C/O = 2.2.

Geometry	$\langle\dot{M}\rangle$ [$M_\odot$/yr]	$\langle v_\infty\rangle$ [km s^{-1}]	$\langle\rho_{\rm d}/\rho_{\rm g}\rangle$
1D (spheric. sym.)	7.9(−6)	31.7	3.2(−3)
2D (axisymmetric)	5.6(−6)	29.2	3.2(−3)

The sudden radiative acceleration of the newly formed dusty regions leaves behind temporary gaps in the dust formation zone which are not only refilled by dust-free matter streaming in from the stellar atmosphere, but also by infalling matter falling back from the outside. These two streams collide in the dust formation zone, which creates turbulence. This turbulence provides additional reasons for the subsequent formation of inhomogeneous dust distributions (Helling et al. 2004).

Furthermore, the infalling matter may already contain some small amounts of dust particles which have been created by nucleation farther out. In this way, dust particles reach again the much denser dust formation zone, where they will serve as additional nucleation seeds. This process results to be the main cause for new dust formation events. Considering the history of sample grains, we find typically

$$\text{nucleation} \rightarrow \text{infall} \rightarrow \text{growth} \rightarrow \text{acceleration}.$$

Last but not least, the more distant dust shells and arcs exhibit a variety of small-scale sub-structures. These small-scale structures are the result of the action of various flow instabilities, not only the Rayleigh-Taylor instability as briefly explained in Sect. 3.2.1. These instabilities apparently need some time to amplify perturbations and so to further shape and fragment the outward moving dust shells and arcs. The result are cauliflower-like shapes, which could also be described as numerous small-scale clouds within the expanding dust shells and arcs.

3.2.3. Comparing 1D with 2D results

Considering the calculated mean wind quantities (e.g. the mass loss rate), the results of the 1D and 2D models are remarkably similar (see Table 3), despite all the detailed effects described in Sect. 3.2.2. The slightly lower mass loss rate in the 2D model (30%) could indicate that dust arcs are slighly less effective in lifting the dust-poor gas in between out of the gravitational potential of the star than complete dust shells. However, this deviation could also be a simple consequence of the insufficient time given to the 2D model to relax.

The deviations along one specific line of sight, however, may be quite different. Consequently, the spectral appearance of the star can be strongly affected by the deviations from spherical symmetry presented in this paper. This will concern lightcurves, images and visibilities, in particular at short (optical and near infrared) wavelengths, where the flux consists mainly of dust attenuated stellar photons. These effects need to be further investigated in a forthcoming paper.

4. Summary and discussion

New axisymmetric (2D) hydrodynamical models for carbon-rich AGB star winds have been developed which include coupled grey continuum Monte Carlo radiative transfer, equilibrium chemistry, time-dependent dust formation and radiation pressure on dust. According to our knowledge, this is actually the first successful application of the Monte Carlo radiative transfer technique in the frame of multi-dimensional hydrodynamical simulations.

The spherical symmetric (1D) version of the code has been checked against other published works (Fleischer et al. 1995; Höfner et al. 1995) showing good agreement in qualitative wind behaviour and quantitative results. Considering the most simple case without stellar pulsation (hydrostatic inner boundary condition), the 1D simulations reveal 3 basic types of dust-driven stellar winds: *stationary winds* with low mass-loss rates and low but supersonic outflow velocities, *oscillating winds* with shock waves and dust shells, high mass-loss rates and high outflow velocities, and *oscillating low-velocity outflows* with low mass-loss rates and sometimes even subsonic outflow velocities.

All three types of dust-driven winds may occur for the same stellar parameters $M_\star$, $L_\star$ and $T_{\rm eff}$ if the carbon-to-oxygen ratio C/O is considered as free parameter. The dependence of wind type (and resultant wind properties) on C/O is found to be *non-unique*, i.e. dependent on history. By increasing C/O, we find a sudden jump from stationary to oscillating wind solutions, whereas for decreasing C/O, we find a sudden jump from oscillating winds to oscillating low-velocity outflows. This *folding bifurcation* (hysteresis behaviour) has not been reported so far. The third type of wind solution (the oscillating low-velocity outflows) seem to resemble the B-type wind solutions proposed by Winters et al. (2002), although we have not considered any stellar pulsation in this paper.

The possibility of a star with given parameters $M_\star$, $L_\star$, $T_{\rm eff}$ and C/O to produce two different types of winds with high and low mass-loss rates might open up the possibility of spontaneous or induced switches between these two mass-loss modes, which could be related to the observation of distant radial dust shells (see e.g. Mauron & Huggins 1999). A mechanism to obtain such switches has been reported by Simis et al. (2001).

The results of the new axisymmetric (2D) dust-driven wind models reveal an even more complex picture of the dust and wind formation around carbon-rich AGB stars. Although the

calculated mean wind properties like $\langle \dot{M} \rangle$ and $\langle v_\infty \rangle$ of the new 2D wind models are rather similar to those of the 1D models, the details exhibit several new effects.

Despite the spherically symmetric initial and boundary conditions, spontaneous symmetry breaking occurs in these winds due to action of various instabilities. Dust is found to form from time to time in restricted regions above the stellar surface. These spatially restricted dust formation events lead to the production of incomplete dust shells, dust arcs or even smaller dust caps. Only in those cases where the complete dust formation zone around the star performs a concerted radial oscillation, a complete dust shell is produced.

The opaque but geometrically thin dust structures are accelerated outward by radiation pressure, expanding radially and tangentially like mushroom clouds, which leads to an accumulation of overlapping arcs in the more distant regions. The optically thin, dust-poor matter in between tends to fall back toward the star, not only temporally (between the active dust formation phases) but also spatially (between the outward moving dusty structures). This matter mixes with fresh dust-free matter from the stellar atmosphere in a turbulent way in the dust formation zone, which again leads to a subsequent production of irregular dust structures.

Further away from the star, flow instabilities (e.g. Rayleigh-Taylor) have time to modify and fragment the outward moving dust arcs and shells, producing numerous small-scale clumps in the outward moving dust shells and arcs.

From the few models calculated so far, we conclude that whenever the 1D model relaxes to an irregular oscillatory wind solution, the 2D model is likely to show strong deviations from spherical symmetry. This type of solution is typical for optically thick winds of embedded IR carbon stars. In contrast, if the 1D model relaxes toward a stationary wind solution (which is the typical result for optical carbon stars with optically thin winds), the 2D model shows a similar behaviour.

The formation of incomplete shells, arcs or smaller caps due to an irregular dust production of the central star may be important to understand recent interferometric observations of embedded carbon stars and red supergiants (e.g. Monnier et al. 2004), which show obvious deviations from spherical symmetry. Woitke & Quirrenbach (2005) have calculated IR images and visibilities from the calculated 2D models discussed in this paper[4] which can be useful for the interpretation of such observations.

Acknowledgements. I want to express my gratefulness to the Leiden theory group around V. Icke for the support of my work. In particular, I want to thank E.-J. Rijkhorst for introducing me to the FLASH-code and S.-J. Paardekooper for correcting the manuscript. This work is part of the ASTROHYDRO3D initiative supported by the NWO COMPUTATIONAL PHYSICS PROGRAMME, grant 614.031.017. The computations have been done on the SARA massive parallel computers in Amsterdam, grant SG-184. The software used in this work was in part developed by the DOE-supported ASCI/Alliance Center for Astrophysical Thermonuclear Flashes at the University of Chicago.

References

Bowen, G. H. 1988, ApJ, 329, 299
Deuflhard, P., & Nowak, U. 1987, Prog. Sci. Comp., 7, 37
Dominik, C., Sedlmayr, E., & Gail, H.-P. 1993, A&A, 277, 578
Fleischer, A. J., Gauger, A., & Sedlmayr, E. 1992, A&A, 266, 321
Fleischer, A. J., Gauger, A., & Sedlmayr, E. 1995, A&A, 297, 543
Freytag, B., & Höfner, S. 2003, poster contribution at International Scientific Meeting of the Astronomische Gesellschaft, September 15–19, 2003, Freiburg, Germany, AG abstract series, 20
Fryxell, B., Olson, K., Ricker, P., et al. 2000, ApJ, 131, 273
Gauger, A., Gail, H.-P., & Sedlmayr, E. 1990, A&A, 235, 345
Gail, H.-P., Keller, R., & Sedlmayr, E. 1984, A&A, 133, 320
Gail, H.-P., & Sedlmayr, E. 1985, A&A, 148, 183
Gail, H.-P., & Sedlmayr, E. 1988, A&A, 206, 153
Grevesse, N., & Noels, A. 1993, in Origin and evolution of the elements (Cambridge: University Press), 14
Habing, H. 1996, A&ARv, 7, 97
Helling, Ch., Klein, R., Woitke, P., Nowak, U., & Sedlmayr, E. 2004, A&A, 423, 657
Höfner, S., Feuchtinger, M. U., & Dorfi, E. A. 1995, A&A, 297, 815
Höfner, S., Fleischer, A. J., Gauger, A., et al. 1996, A&A, 314, 204
Höfner, S., Gautschy-Loidl, R., Aringer, B., & J/orgensen, U. G. 2003, A&A, 399, 589
Jura, M., Chen, C., & Plavchan, P. 2002, ApJ, 569, 964
Le Bertre, T. 1997, Lecture Notes in Physics, ed. J.-P. De Greve, R. Blomme, & H. Hensberge (Springer), 497, 133
Lucy, L. B. 1971, ApJ, 1971, 163
Mauron, N., & Huggins, P. J. 1999, A&A, 349, 203
Monnier, J. D., Millan-Gabet, R., Tuthill, P. G., et al. 2004, ApJ, 605, 436
Niccolini, G., Woitke, P., & Lopez, B. 2003, A&A, 399, 703
Pascucci, I., Wolf, S., Steinacker, J., et al. 2004, A&A, 417, 793
Rijkhorst, E., Plewa, T., Dubey, A., & Mellema, G. 2005 [arXiv:astro-ph/0505213]
Sandin, C., & Höfner, S. 2003, A&A, 404, 789
Schirrmacher, V., Woitke, P., & Sedlmayr, E. 2003, A&A, 404, 267
Simis, Y. J. W., Icke, V., & Dominik, C. 2001, A&A, 371, 205
Tuthill, P. G., Monnier, J. D., & Danchi, W. C. 2005, ApJ, 624, 352
Wallerstein, G., & Knapp, G. R. 1998, ARA&A, 36, 369
Weigelt, G., Balega, Y. Y., Blöcker, T., et al. 2002, A&A, 392, 131
Winters, J. M., Le Bertre, T., Jeong, K. S., Helling, Ch., & Sedlmayr, E. 2000, A&A, 361, 641
Winters, J. M., Le Bertre, T., Nyman, L.-Å., Omont, A., & Jeong, K. S. 2002, A&A, 388, 609
Woitke, P. 1999, in Astronomy with Radioactivities, ed. R. Diehl, & D. Hartmann, Schloß Ringberg, Germany: MPE Report, 274, 163
Woitke, P., Sedlmayr, E., & Lopez, B. 2000, A&A, 358, 665
Woitke, P., & Niccolini, G. 2005, A&A, 433, 1101
Woitke, P., & Quirrenbach, A. 2005, in The Power of Optical/IR Interferometry: Recent Scientific Results and 2nd Generation VLTI Instrumentation, ed. F. Paresce, & A. Richichi (Springer-Verlag), in press
Woitke, P., Farzinnia, A., & Weterings, M. 2006, A&A, in prep.

[4] See http://www.strw.leidenuniv.nl/~woitke for mpeg-animations and simulated images.